Partial nitridation-induced electrochemistry enhancement of ternary oxide nanosheets for fiber energy storage device

Hao, Pin; Tan, Hua; Liu, Zhihe; Chao, Dongliang; Jia, Dedong; Sang, Yuanhua; Liu, Hong; Fan, Hong Jin

2018

Tan, H., Liu, Z., Chao, D., Hao, P., Jia, D., Sang, Y., . . . Fan, H. J. (2018). Partial nitridation-induced electrochemistry enhancement of ternary oxide nanosheets for fiber energy storage device. Advanced Energy Materials, 8(21), 1800685-. doi:10.1002/aenm.201800685

https://hdl.handle.net/10356/82496

https://doi.org/10.1002/aenm.201800685

Partial Nitridation Induced Electrochemistry Enhancement of Ternary Oxide Nanosheets for Fiber Energy Storage Device

By Hua Tan, Zhihe Liu, Dongliang Chao, Pin Hao, Dedong Jia, Yuanhua Sang, Hong Liu, and Hong Jin Fan**

H. Tan, Z. Liu, Y. Sang, Prof H. Liu*

State Key Laboratory of Crystal Material, Shandong University, Jinan 250100, PR China.

E-mail: hongliu@sdu.edu.cn

H. Tan, Dr. D. Chao, Prof. H. J. Fan*

School of Physical and Mathematical Sciences, Nanyang Technological University, 637371, Singapore

Email: fanhj@ntu.edu.sg

Prof H. Liu*

Institute of Advanced Interdisciplinary Research (IAIR), University of Jinan, Shandong 250022, China

P. Hao

College of Chemistry, Chemical Engineering and Materials Science, Shandong Normal University, Jinan 2 50014 (China)

D.D. Jia

School of Material Science and Engineering, Qingdao University, 308 Ningxia Road, Qingdao, Shangdong, P.R.C, 266071

Keywords: fiber-based power source, flexible energy storage, metal nitride array, hybrid battery, solid state supercapacitor

Abstract

Fiber-based power sources are receiving interests in application in wearable electronic devices. Herein, we fabricate fiber-shaped all-solid-state asymmetric energy storage devices based on a partially nitridized $NiCo_2O_4$ hybrid nanostructures on graphite fibers. The surface nitridation leads to a three-dimensional (3D) "pearled-veil" network structure, in which Ni-Co-N nanospheres are mounted on $NiCo_2O_4$ nanosheets electrode. We demonstrate that the hybrid materials are more potent than the pure $NiCo_2O_4$ in energy storage applications due to cooperative effect between the constituents. The Ni-Co-N segments augments the pristine oxide nanosheets by enhancing both capacity and rate performance (specific capacity of 384.75 mAh/g at 4A/g, and a capacity retention of 86.5% as the current is increased to 20 A/g). The whole material system has a metallic conductivity that renders high-rate charge and discharge, and an extremely soft feature so that it can wrap around arbitrary-shape holders. We fabricate all-solid-state asymmetric device using Ni-Co-N/$NiCo_2O_4$/GFs and CNTs/GFs as the electrodes. The flexible device delivers outstanding performance compared to most oxide-based full devices. This structured hybrid materials may find applications in miniaturized foldable energy devices.

Introduction

In recent years, high-efficiency electrical energy storage and conversion devices have drawn intensive attention due to the ever-growing demand for sustainable energy.[1, 2] Supercapacitors as one of the most practical and effective techniques for electrochemical energy storage have been extensively investigated due to their advantageous features of fast charging/discharging rate, high power density, long cycle life, and flexibility. However, the low energy density is still the main drawback of the supercapacitor for competing with the batteries. During the past few years, there is a dramatic expansion in research towards hybrid supercapacitor combined with a faradaic and a capacitor-type electrode.[3] Battery-like (faradaic) electrodes have been widely investigated as the energy source of the capacitors.[4] Such electrodes can achieve battery-level energy density while maintain a capacitor-level long life and good rate capability.[2, 5] $NiCo_2O_4$ has been widely investigated as a battery-like electrode owing to the superior redox activity and high theoretical capacity compared to single-component oxide/hydroxides.[6] However, this kind of surface Faradaic reaction dominated materials still suffer from low rate capability and/or poor electrochemical stability due to the poor intrinsic conductivity and extra contact resistance. Consequently, many efforts have been paid on conductivity enhancement by surface coating with carbonaceous materials (e.g. graphene nanosheets) or synthesizing metal oxide heterostructures.[7-10] However, the improvement is still limited, partly because these composites may have unfavorable reaction kinetics that limit the multi-ion or multi-electron involved surface redox reactions.[11]

Metal nitrides generally have a metallic conductivity (4000~55500 S/cm),[12] and thus are suitable for electrochemical energy storage. For example, many metal nitrides, such as TiN,[8, 13] VN,[14] Mo_2N,[15] and FeN,[16] are commonly used as the electrode materials in supercapacitors or lithium ion batteries. The other advantage of metal nitrides is their lower reduced states than oxides, which in principle can render more faradic charges and higher specific capacitance if the redox reactions are reversible. The metal cation valence states in nickel and cobalt nitrides (for example, Ni_3N and CoN) are lower than in oxides.[17] Hence, they can exhibit higher reactivity than the corresponding pure metals or metal oxides. Nonetheless, in the case of nickel cobalt nitride related hybrid electrodes nitride-based hybrid electrodes, it is still necessary to further enhance the charge transport and redox reactivity.

Recently, solid-state energy storage device based on fiber electrodes have been explored extensively to meet the demand for flexible and wearable electronic devices.[18] Graphite fibers (GFs) integrate multiple features such as high mechanical flexibility, electrical and thermal conductivities, which make

them more useful than conventional carbon cloth (Fig. S1). It is highly interesting to construct fiber-shaped supercapacitors or batteries based on such GFs,[19] as the device can be bendable, twistable or woven into fabrics.

Based on the above considerations, herein, we aim to develop flexible power devices based on rationally designed bimetallic metal nitride electrodes on graphite fibers (see schematics in Fig. 1). Our electrode contains Ni-Co-N nanospheres (specifically, CoN and Ni_3N) anchored within a network of bimetallic oxide nanosheets on GFs. The pre-grown $NiCo_2O_4$ nanosheets are subject to thermal annealing in an ammonia ambient. During the annealing process, Ni-Co-N nanospheres are formed in situ on $NiCo_2O_4$ nanosheets and form a 3D "pearled-veil" structure (Ni-Co-N/$NiCo_2O_4$/GFs). In this design, the electrochemical contributions from both nickel and cobalt ions in the bimetallic nitrides can provide rich redox reactions, resulting higher capacity. The 3D configuration can prevent the possible aggregation and metal nitride surface oxidation of the active materials during the repeated discharging and charging reactions. In the meantime, the treatment also results in vacancies in the oxides and extends reaction activity. Therefore, the resultant Ni-Co-N/$NiCo_2O_4$/GFs electrode possesses an obviously improved performance as a battery-like electrode compared to the pristine $NiCo_2O_4$ nanosheets in capacity (384.75 mAh/g at 4A/g), rate capability (86.5% capacitance retention 4-20A/g) and lifespan (92% capacitance retention for 10000 cycles). Our work sheds light on the rational structural engineering of electrodes to improve performance of energy storage devices.

Results and discussion

Microstructure and composition characterization. The morphology of the samples at different fabrication stages are observed by scanning electron microscopy (SEM). Apparently, the pristine GFs showed the clean but rugged surface, which is benefit to the electrodeposition process (Fig. S1 inset). The representative SEM images in Fig 2 (a) reveals that, before annealing in the ammonium, numerous nanosheets cover homogeneously on the surface of GFs. And since their interconnected loose porous nanostructures, abundant open space and electroactive surface sites are provided. The distance between each pair of neighboring sheets (around 200 nm) is beneficial to the nitridation process in the following steps. In order to reveal more structural information, TEM characterization was carried out. The low-magnification TEM image in Fig. S3 (a) elucidates the nanosheets have a porous structure with 2-5nm size pores (Fig. 2(b)). The lattice fringes shown in Fig. 2 (c) can be readily indexed to the (220) and

(111) crystal planes of the cubic $NiCo_2O_4$ phase. After calcining at 400 ℃ in the ammonium atmosphere, large amounts of nanospheres distribute uniformly on both sides of the nanosheets (Fig 2 (d) and Fig. S3(b)), forming a 3D "pearled-veil" nanostructure on the surface of GFs (Fig. S 2(a)). From the cross section of the fibrous hybrid sample, it is found that the nanosheets interconnect together and tightly grow on the GFs with thickness about 300 nm (Fig. S2 (b) and (c)). An enlarged view in Fig. 2 (e) and (f) reveals that the nanospheres have the size range from 10 to 50 nm. The lattice fringes for the nanospheres show inter planar spacing of 0.248 and 0.203 nm, corresponding to the (111) planes of the CoN and Ni_3N, respectively. Meanwhile, lattice fringes obtained from the remaining nanosheets show an inter planar spacing of 0.245 nm, corresponding to the (311) planes of the $NiCo_2O_4$. Furthermore, the 3D configuration of Ni-Co-N/$NiCo_2O_4$ hybrid was also verified by EDX mapping (Fig. 2 (g)). The unique hybrid structure with a high Brunauer-Emmett-Teller (BET) specific surface area (Fig. S3 (c)) endows the Ni-Co-N/$NiCo_2O_4$/GFs with abundant open space and a continuous pore size range (Fig. S3 (d)). This implies a large number of surface sites for electrochemical reactions and facile ion diffusion.

Consistent with the HR-TEM characterization in Fig. 2(c) and (f), the XRD spectrum in Fig. 3 (a) of the $NiCo_2O_4$/GFs can be well indexed to $NiCo_2O_4$ (JCPDS card no. 73-1702). After nitridation in ammonium, two dominating peaks at 36.1 ° and 44.5 ° are indexed to the (111) plane of the CoN (JCPDS Card no. 83-0831) and Ni_3N (JCPDS Card no. 10-0280), respectively. Weak peaks at 36.7 ° of (311) plane of the $NiCo_2O_4$ still exist. The peak observed at 26.4°, both in the $NiCo_2O_4$/GFs and Ni-Co-N/$NiCo_2O_4$/GFs, is ascribed to the (002) plane of the hexagonal graphite structure, indicative of the presence of graphite species. Fig. 3 (b)-(d) show the X-ray photoelectron (XPS) measurements, which confirms the existence of Ni, Co and N elements within the as-prepared Ni-Co-N/$NiCo_2O_4$/GFs and provide more detailed information about their oxidation states. By applying a Gaussian fitting method, the Ni 2p spectra can be well-fitted with two spin-orbit doublets, assigned to the presence of Ni^+/Ni^{2+}/Ni^{3+} due to the formation of Ni_3N and the retained $NiCo_2O_4$ in the Ni-Co-N/$NiCo_2O_4$.[20, 21] In this case, the Ni^+ represents the mixed state between Ni^0 and Ni^{2+}, which is the mixed valence owning to the co-existence of Ni_3N and CoN. Besides, the Ni 2p spectrum contains two prominent shake-up satellites (denoted as "Sat.").[22] The intensity of the Ni^{2+} and Ni^{3+} peaks in Ni-Co-N/$NiCo_2O_4$/GFs are lower than that of the $NiCo_2O_4$/GFs (Fig. S4(a)). For Co 2p XPS spectrum of the Ni-Co-N/$NiCo_2O_4$/GFs (Fig. 3 (c)), the co-existence of the Co^{2+} and Co^{3+} is attributed to the non-metering hybrid valence state

due to the formation of the CoN and little retained $NiCo_2O_4$ oxides. The intensity variety of the Co^{3+} and Co^{2+} compared with the $NiCo_2O_4$/GFs (Fig. S 4(b)) indicates the dominance of the nitride in the hybrid structures, which is consistent with the above results. The high resolution of N1s spectrum (Fig. 3(d)) reveals the formation of metal nitride nitrogen and pyrrolic nitrogen in the Ni-Co-N/$NiCo_2O_4$/GFs.[20, 23] For the O1s high resolution spectrum, comparing with the $NiCo_2O_4$/GFs, the O 1 (529.89 eV) for the Ni-Co-N/$NiCo_2O_4$/GFs decreases significantly. The smaller but finite intensity of the O1 peak is due to the retained $NiCo_2O_4$ nanosheets, the O2 peak (531.2 eV) attributed to oxygen vacancies has a relative larger intensity than the other two oxygen peaks. Meanwhile, the X-ray absorption near edge spectroscopy (XANES) measurements at the Ni and Co K-edge were also carried out to further certify the constituent of the $NiCo_2O_4$/GFs and Ni-Co-N/$NiCo_2O_4$/GFs samples. As shown in Fig. 3 (e), the lower energy shifting and intensity increasing for Ni-Ni peaks demonstrate the Ni in Ni-Co-N/$NiCo_2O_4$/GFs is more readily reduced to a lower valence state and thus, the metallicity of the sample increases. Fourier transformed extended XAFS (FT-EXAFS) (Fig. 3 (f)) data for Ni-Co-N/$NiCo_2O_4$/GFs and $NiCo_2O_4$/GFs were further used to verify the valence state. The results confirm the existence of Ni^+ and also prove that the formation of metal nitride reduces the coordination ability of metal-oxygen bonds, enhancing the relative content of vacancies. The result is consistent with the XPS results. The Co K-edge energies have the similar tendency with the Ni K-edge, and the oxidation state of Co in Ni-Co-N/$NiCo_2O_4$/GFs is close to that of CoN. Furthermore, the partial doping of Ni at the Co site makes the Co K-edge energy slightly shift towards lower value and the Co state valence become closer to Co^{2+}, which is consistent with the XPS results (the proportion of Co^{2+} increased) (all the detailed information can be found in Fig. S4).

Since the formation of the Ni-Co-N nanospheres is critical to the final Ni-Co-N/$NiCo_2O_4$/GFs architecture, temperature dependent experiments have been conducted to obtain a better insight to the evolution process of the Ni-Co-N/$NiCo_2O_4$/GFs. The $NiCo_2O_4$/GFs after nitridation at different reaction temperatures are also studied in the paper. According to the SEM images (Fig. S5), XRD patterns (Fig. S6) and XPS (Fig. S7) spectrum, the formation of the Ni-Co-N/$NiCo_2O_4$/GFs hybrid is a temperature dependent process and the hybrids will have the most ideal morphology and strong adhesion on the fibers only nitriding at 400 ℃. For the detailed information, please refer to related supporting information.

Performance enhancement in hybrid structure. The electrochemical performances of the

$NiCo_2O_4$/GFs and Ni-Co-N/$NiCo_2O_4$/GFs were investigated by directly using the fibrous samples as working electrodes in a three-electrode cell in the 3 M KOH aqueous electrolyte (Fig. 4). The bare GFs substrate shows a smaller current response in comparison with that of the $NiCo_2O_4$/GFs and Ni-Co-N/$NiCo_2O_4$/GFs (Fig. S8 (a)), indicating the negligible contribution of the GFs towards the capacitance. The cyclic voltammetry (CV) curves show the battery-type characteristics derived from Faradic reactions of the $NiCo_2O_4$/GFs and Ni-Co-N/$NiCo_2O_4$/GFs. Furthermore, the area integrated within the current-potential curve for the Ni-Co-N/$NiCo_2O_4$/GFs 400 ^oC is much larger than that of the $NiCo_2O_4$/GFs, indicating the Ni-Co-N/$NiCo_2O_4$/GFs electrode has higher electrochemical reaction activity. Fig. 4 (a), and (c) further demonstrate the representative CV curves of the $NiCo_2O_4$/GFs and Ni-Co-N/$NiCo_2O_4$/GFs electrodes with various sweep rates ranging from 5 to 100 mV/s. As shown in Fig. 4 (a) a pair of redox peaks within -0.1~0.4V (vs. $Ag/AgCl_2$) is observed, indicating the electrochemical capacity of the self-supported mesoporous $NiCo_2O_4$ nanosheets on the GFs is distinct from electric double-layer capacitance characterized by nearly rectangular CV curves due to the Non-faradic reactions. The reactions are mainly corresponded to the reversible reactions of Co^{2+}/Co^{3+} and Ni^{2+}/Ni^{3+} transitions associated with OH^- in the alkaline electrolyte as the following equations:

$$NiCo_2O_4 + OH^- + H_2O \leftrightarrow NiOOH + 2CoOOH + e^-$$

$$CoOOH + OH^- \leftrightarrow CoO_2 + H_2O + e^-$$

With the 20-fold increase in the sweep rate from 5 to 100 mV/s, the position of the cathodic peak shifts ca. 110 mV, which suggests a relatively low resistance of the electrode. After being nitridized in the ammonium atmosphere, the Ni-Co-N/$NiCo_2O_4$/GFs has the more favorable CV curves: both the area and the specific current of the CV curves are larger than that of the $NiCo_2O_4$/GFs. Meanwhile, with the increase of scan rate, the Ni-Co-N/$NiCo_2O_4$/GFs electrodes reveal the battery-type behavior, such as the enhanced redox peak sharpness, smaller peak positions shift (45 mV) compared with that of the $NiCo_2O_4$/GFs, which suggests the hybrid electrode has lower polarization, better conductivity and good faster redox reaction kinetics. The galvanostatic charge/discharge (GCD) curves of the $NiCo_2O_4$/GFs (Fig. 4 (b)) and the Ni-Co-N/$NiCo_2O_4$/GFs (Fig. 4 (d)) are carried out at different current densities (4-20 A/g). As shown in Fig. 4 (b) and (d), the potential-time curves at all current densities are almost symmetric, indicative of a high coulombic efficiency due to the highly reversible redox reactions during the charge/discharge process. Compared with $NiCo_2O_4$ /GFs (Fig. 4 (b)), the Ni-Co-N/$NiCo_2O_4$/GFs (Fig. 4 (d)) has a more obvious plateau corresponding to a more significant battery-type redox behavior.

The specific capacities of the $NiCo_2O_4$/GFs and the Ni-Co-N/$NiCo_2O_4$/GFs calculated from the charge/discharge curves according to equation (2) are plotted in Fig. 4 (e). The Ni-Co-N/$NiCo_2O_4$/GFs electrode exhibits higher specific capacities, ranging from 384.75 mAh/g at the specific current of 4 A/g to 332.73 mAh/g at 20 A/g, corresponding to a capacity retention of 86.5%. For the $NiCo_2O_4$/GFs, the corresponding capacity retention is 76 %. This implies that the hybrid electrode has a higher charge storage properties, better electrochemical reversibility and rate capability than the pure oxide one.

In order to evaluate the charge transport impedance, electrochemical impedance spectroscopy (EIS) was carried out in a frequency range from 0.01 Hz to 100 kHz, and the results are shown in Fig. 4 (f). The equivalent circuit model was introduced to clarify the performance of the electrodes as shown in Fig. S9 (a). In Fig. 4 (f), the equivalent series resistance (R_s) of the $NiCo_2O_4$ /GFs is ca. 0.608 Ω, which is lower than that of the pristine graphite fibers (0.983 Ω, Fig. S9(b)). It indicates that there is a good combination between GFs and $NiCo_2O_4$ nanosheets. After the nitridation process, the Ni-Co-N/$NiCo_2O_4$/GFs electrode exhibits a better conductivity with the R_s of ca. 0.407 Ω. The resistance results combined with the CV and GCD data reveal that the Ni-Co-N/$NiCo_2O_4$/GFs have better electrochemical activity, rapid electro transport kinetics, and fast diffusion of ions at the interface of electrode/electrolyte conductivity and electro-performance than the $NiCo_2O_4$/GFs.

The cycling stability is always an important factor for the solitary Ni-Co-N/$NiCo_2O_4$/GFs electrode. Fig. 4 (g)-(i) showed the cycling stability of the Ni-Co-N/$NiCo_2O_4$/GFs. The specific capacity retention of the hybrid electrode still remained 99.85% after 3000 cycles at 8A/g. There is no significant change in the charge/discharge behavior was observed after the long-term cycles, as show in the inset of Fig. 4 (i). The high-resolution XPS spectra (Fig. 4 (g)-(h) and Fig. S10) of the Ni-Co-N/$NiCo_2O_4$/GFs also shows negligible difference in all the chemical states prior to and after cycling. Hence, it is concluded that the Ni-Co-N/$NiCo_2O_4$/GFs structure has a good chemical stability.

We also measured the electrochemical performance (Fig. S8) and the electrochemical impedance spectroscopy (Fig. S9 (b)) of the Ni-Co-N/$NiCo_2O_4$/GFs obtained from the three annealing temperatures (300, 400, and 500 ^oC). The detailed analysis is presented in Supporting Information. The results imply that the Ni-Co-N/$NiCo_2O_4$/GFs (400 ^oC) has the best electrochemical performance and highest conductivity, which can be ascribed to cooperation effect in the “nitride + oxide hybrid” in the unique 3D “pearled-veil” nanostructure. As we know, the performance of a supercapacitor with nanostructured electrodes depends not only on the material itself, but also other factors such as surface areas, interface

resistance, and transport impedance. In our case, the sample after 500 °C annealing is fully converted to nitrides. However, the whole array structure is damaged, and individual nitride particles severely aggregate and are not in close contact. So its performance becomes worse. As for the 300 °C sample, it is only slightly reduced but not yet fully converted (as seen from XRD data in Figure S6). Some defects are generated on the surface of oxide nanosheets (the O2 peak area increases in the O1s XPS spectra, Figure S7c). Therefore, it is not surprising that the electrochemical performance is only slightly better than the pristine oxides, but still inferior to the optimized sample (400 °C).

We would like to attribute the high electrochemical performance of the Ni-Co-N/$NiCo_2O_4$/GFs (400 °C) electrode to the following key factors: the unique hybrid architecture and the high specific surface area (Fig. S3 (c) and (d)) provide a favorable electron and ion percolation network in the composite, thus reduces the diffusion length of the ions and electrons. Next, we employ the highly conductive GFs as both the self-supported substrate and current collector, and the nickel cobalt nitrides nanospheres in situ formed within the $NiCo_2O_4$ nanosheet network also reduces the internal resistivity. Together with the fact that CoN and Ni_3N have a metallic characteristic,[20, 24] the whole electrode exhibit a very low impedance and can thus render fairly high rate performance. Furthermore, the partial nitridation of the $NiCo_2O_4$ nanosheets increases the level of defects, such as oxygen vacancies (as indicated by XPS and EXAFS results), and thus may have introduced more active sites and lowered the valence states of metal cations. According to Dunn and coworkers, oxygen vacancies in the retained nickel cobalt oxide can act as shallow donors and increase the carrier concentration,[25] leading to faster kinetics and more adequate Faradaic redox process. Therefore, the Ni-Co-N/$NiCo_2O_4$/GFs electrode with the 3D "pearled-veil" nanostructure can demonstrate superior electrochemical performance towards the fabrication of full flexible energy storage devices.

Asymmetric full energy storage device. The above results from three-electrode measurement are useful understanding the fundamental electrochemical behaviors and charge storage abilities of the active materials. However, for the practical applications, two-electrode full cells are necessary to be fabricated and evaluated. Herein, we have assembled asymmetric all-solid-state energy storage devices by employing the Ni-Co-N/$NiCo_2O_4$/GFs as the positive electrode and nitrogen-doped carbon nanotubes/GFs (N-CNTs/GFs) as the negative electrode (Ni-Co-N/$NiCo_2O_4$/GFs||N-CNTs/GFs) in the PVA/KOH electrolyte gel, as shown in Fig. 5 (a). The N-CNTs are grown homogeneously on the surface of GFs by an ambient-pressure chemical vapor deposition at 600 °C followed by ammonium calcination.

The morphology and electrochemical performance of the N-CNTs/GFs are presented in Fig. S11. The N-CNTs/GFs electrodes have a typical double layer capacitance characteristic, with weak redox peaks in the CV curves due to the nitrogen doping in the CNTs.

For the full cell, the optimal mass ratio of positive-to-negative electrodes is determined to be 0.205 (based on Eq. 5), and the voltage window is determined to be 1.8 V according to their individual electrochemical behaviors (Fig. S12 (a)). The expansion of the voltage window is mainly related to the higher electrical conductivity and weaker polarization of Ni-Co-N in the solid electrolyte compared to the aqueous KOH. As shown in Fig. 5 (b), the CV curves at various scan rate demonstrate that the as-fabricated asymmetric full device shows an excellent capacitive behavior at 0-1.8 V. Moreover, at the same scan rate, the device has larger CV integral area than that of the control cell of $NiCo_2O_4$/GFs||N-CNTs/GFs (Fig. S12 (b)). As shown in Fig. 5(c), the galvanostatic charge/discharge (GCD) curves at all specific currents are almost symmetric, indicative of a high coulombic efficiency and good capacitive characteristics of the solid-state device. Our device is more like a battery-type capacitor according to the CV and GCD behavior. Specific capacities of the $NiCo_2O_4$/GFs||N-CNTs/GFs and the Ni-Co-N/$NiCo_2O_4$/GFs||N-CNTs/GFs are summarized in Fig. S12 (d). The Ni-Co-N/$NiCo_2O_4$/GFs||N-CNTs/GFs device delivers high specific capacity values of 139.88 and 108.56 mAh/g at 4 and 40 A/g, respectively, suggests that about 78% of the capacity is retained when the charge-discharge current increases by 10 times. In contrast, for the control device of $NiCo_2O_4$/GFs||N-CNTs/GFs, the specific capacity values are much lower: 98.55 and 45.07 mAh/g at the same specific current range from 4 to 40 A/g, corresponding to a lower capacity retention of about 46%. The EIS results in Fig. S12 (e) indicates its lower charge transfer and diffusion resistance of the Ni-Co-N/$NiCo_2O_4$/GFs||N-CNTs/GFs device than the $NiCo_2O_4$/GFs||N-CNTs/GFs, which accounts for the excellent rate capability in the former cell.

Long cycle life and high specific power and energy are required for practical applications of energy storage devices. The long-term cycling performance of the electrodes at a constant specific current of 8 A g^{-1} is shown in Fig. 5 (d). Interestingly, the capacity of the Ni-Co-N/$NiCo_2O_4$/GFs||N-CNTs is rather stable after continuous charge/discharge for 10000 cycles with a retention of about 92%. The GCD curves also show insignificant change after the long-term cycles compared to the $NiCo_2O_4$/GFs||N-CNTs device (retention is about 77%), as shown in Fig. S12 (f). Such an excellent cycle performance stems from the high conductivity of Ni_3N and CoN and the presence of $NiCo_2O_4$ nanosheets which is

helpful to maintain the structural integrity and electrochemical activity of Ni-Co-N.

For the asymmetric devices, the specific energy and power were calculated from galvanostatic discharge curves according to equation (3), (4) and plotted on the Ragone diagram shown in Fig. 5 (e). Note that only the mass of active materials are included in the calculation for pair comparison to other devices. The Ni-Co-N/$NiCo_2O_4$/GFs‖N-CNTs has a maximum specific energy of 125.89 Wh/kg at 1.68 kW/kg and highest specific power of 36.23 kW/kg at 82.42 Wh/kg. These results are much better than those of the $NiCo_2O_4$/GFs‖N-CNTs devices (88.69 Wh/kg at 1.18 kW/kg) and some reported values in the literature(such as AC‖rGO/MnOx,[26] Ni-Co-S/G‖PCNS,[7] Co_3O_4/VAGN/CF‖Co_3O_4/VAGN/CF,[9] Gr/MnO_2‖Gr/MnO_3,[27] $NiCo_2O_4$/3D-G‖3D-G,[28] Ni, Co-OH/rGO‖HPC,[29] Ni-Cd batteries[30] and $NiCo_2S_4$/PPy-50‖AC[31]). The resultant Ragone plots of our asymmetric device and the aforementioned symmetric or asymmetric cells are shown in detail in Fig. 5 (e) and Table. S1.

Finally, we present the flexibility property. The as-integrated $NiCo_2O_4$/Ni-Co-N/GFs‖N-CNTs asymmetric devices was subject to bending at different angles (data presented in Fig. 5 (f)). It is shown that the full devices can be folded to arbitrary shapes similar to the pristine GFs (Fig. 1 (c)). There is no apparent specific capacity loss (Fig. 5 (f)) or shape change in CV curves (Fig. S 13 (a)) prior to and after the bending, indicating the good electrochemical durability and flexibility of the device. As a proof-of-concept demonstration of the potential application, two devices in series can power a light-emitting diode (LED) indicator (3 V) after being charged at 4 A/g (Fig. S13 (b)). All in all, our two-electrode asymmetric device made of Ni-Co-N/$NiCo_2O_4$/GFs‖N-CNTs/GFs shows a high specific energy and outstanding stability. More importantly, our material design concept (3D 'nitride+oxide hybrid' by partial nitridation) may be extended to engineering other different metal compounds based electrodes for performance enhancement.

Conclusion

We have demonstrated the effectiveness of enhancing the electrochemical energy storage performance of $NiCo_2O_4$ nanosheets by partial nitridation to introduce oxygen vacancies, increase active sites and electrical conductivity. The formed Ni-Co-N nanospheres entangled with remaining $NiCo_2O_4$ nanosheets form a 3D "pearled-veil" hybrid structure on graphite fibers. The entire fibrous electrode, containing graphite fibers, porous $NiCo_2O_4$ nanosheets and Ni-Co-N nanospheres show a metallic conductivity, and thus is an excellent candidate for capacitive energy storage. Indeed, the

obtained Ni-Co-N/$NiCo_2O_4$/GFs demonstrate much superior performance than the pristine $NiCo_2O_4$ nanosheet based one, in terms of specific capacity, rate performance and cycle stability. For a proof-of-concept demonstration, we have fabricated solid-state asymmetric energy devices based on the soft fibrous electrodes, which are fully bendable and tailorable. The device shows a maximum specific energy of 125.89 Wh/kg and highest specific power of 36.23 kW/kg, proving its application potential in flexible and lightweight electronics.

Experimental Section

Chemicals. The graphite fibers (M40-JB-12K,) were obtained from Toray (Japan). All other chemicals (such as the $NiCl_2.6H_2O$, $CoCl_2.6H_2O$, acetone and ethanol) are of reagent grade and used without further purification. Deionized water was used throughout the experiments.

Material preparation. Briefly, graphite fibers were sequentially treated by sonicating in acetone and ethanol in sequence for 10 min to remove the surface impurities, and then rinsed with deionized water. The electrodeposition process was carried out in the standard three-electrode cell system by using fibrous sample as work electrode, platinum plate counter electrode, and a saturated calomel reference electrode (SCE). The bimetallic solution is constituted of 6 mM $CoCl_2.6H_2O$ and 3 mM $NiCl_2.6H_2O$. The electrodeposition potential was -1.0 V (vs. SCE) and the deposition time was 5 min. The fabrication process for the electrode material is shown schematically in Fig. 1. The obtained precursor was calcined at 350 ℃ for 2 h with a ramping rate of 2 ℃/min to obtain the porous nanosheets of $NiCo_2O_4$/GFs. Finally, the $NiCo_2O_4$/GFs were annealed in the NH_3 atmosphere for 2 h with a ramping rate of 3 ℃/min under 400 ℃ to form the Ni-Co-N/$NiCo_2O_4$/GFs.

Material characterization. The morphology and the microstructure of all the samples at different processing stages were characterized using HITACHIS-4800 field-emission scanning electron microscope (FE-SEM) and high-resolution transmission electron microscope (HR-TEM, JEM 2100F). The surface chemical species of the samples were determined with a PHI 5000 Versa Probe X-ray photoelectron spectrometer (XPS). X-ray powder diffraction (XRD) patterns were recorded on the Bruker D8 Advance powder X-ray diffractomer with Cu-Kα radiation (λ=0.15406 nm). The absorption spectra of Ni K-edge and the Co K-edge were collected in transmission mode using a Si (111) double-crystal monochromator at the X-ray absorption fine structure (XAFS) station of the 1W1B beamline of the Beijing Synchrotron Radiation Facility (BSRF). The electrical transport property measurements were carried out on pressed pellets using a Keithley 4200-SCS semiconductor characterization system and the four-point probe method. Our first-principles calculations were performed within density-functional theory (DFT) using the Vienna ab initio simulation package known as the VASP code. The projector augmented wave method (PAW) was used to describe the electronic-ion interaction. The energy cutoff of the plane waves was set to 450 eV with an energy precision of 10^{-5} eV. The electron exchange–correlation function was treated using a generalized gradient approximation (GGA) in the form proposed by Perdew, Burke, and Ernzerh of (PBE). The method of LDA+U, The U value for Co and Ni taken from the previous work are 6.7 and 7.1 respectively. The Monkhorst-Pack k-point meshes for the Brillouin zone (BZ) sampling are well converged for each system.

Electrochemical measurements. In this section, both three-electrode and two-electrode configurations were used to study the electrochemical properties of the samples on a CHI660E electrochemical workstation (Shanghai Chen Hua Instruments Co., China). The test was carried out in 3 M KOH solution at room temperature. In the three-electrode system the self-supported binder free Ni-Co-N/$NiCo_2O_4$/GFs were used as the work electrode, a Pt with a size of 1×1 cm^2 served as counter electrode and a Ag/AgCl electrode (saturated KCl) as reference electrode. The electrochemical impedance spectroscopy (EIS) measurements were carried out in the frequency range from 10 mHz to 100 kHz at open circuit potential. The two-electrode system was used to evaluate the performance of the all-solid-state energy storage device with KOH/PVA gel as the electrolyte. To prepare the KOH/PVA gel electrolyte, 6 g of KOH was added to 60 mL of deionized water and 6 g of PVA was then added. The mixture was then heated to 85 °C under continuous stirring until the solution became clear. Two electrodes were immersed into the KOH/PVA solution for 10 min, and then solidified at room temperature. The cycling performance of the materials was measured with a Gamry 3000 electrochemical workstation (USA).

Calculations of specific capacity, energy density and power density. Typically, for the three-electrode system, we calculated the specific capacity of the electrodes according to the CV curves based on the following equation:

$$Cs = \frac{1}{3.6}\frac{\mathrm{Q}}{\mathrm{m}v} = \frac{1}{3.6}\frac{\int IdU}{2mv} \quad (1)$$

Cs (mAh/g) is the specific capacity, Q (C) is the average charge, v is the scan rate and m is the active material mass of the working rode. As for the two-electrode system m is the total mass loading of the two electrodes.

Specific capacities of the electrodes were calculated according to the charge/discharge curves based on the following equation:

$$C_s = \frac{1}{3.6}\frac{\int Idt}{\mathrm{m}} \quad (2)$$

where C_s (mAh/g) is the specific capacity, I_d (mA) is the discharge current, Δt (s) is the discharge time, m (mg) is the mass loading of the active material on a single electrode.

The energy density (E, Wh/Kg) and power density (P, W/Kg) of the active materials were calculated from galvanostatic charge/discharge testing based on the following equation:

$$\mathrm{E} = \frac{1}{2}C_s \times \Delta V \quad (3)$$

$$\mathrm{P} = \frac{3.6E}{\Delta t} \quad (4)$$

where Cs (mAh/g) is the specific capacity based on the two electrodes, ΔV (V) is the discharge voltage range exclusive of the IR drop and Δt(s) is the discharge time.

The mass ratio of the two electrode materials was balanced before making the asymmetric energy storage devices by means of the following relationship:

$$\frac{m_+}{m_-} = \frac{C_-V_-}{C_+V_+} \quad (5)$$

where m_+ is the mass, C_+ is the specific capacity, V_+ is the working voltage of the positive electrode, and V_-, m_-, and C_- are the working voltage, mass, and specific capacity of the negative electrode, respectively.

Acknowledgements

H. Tan and Z.H. Liu contribute equally to this work. The authors are thankful to funds from the National Natural

Science Foundation of China (Grant No. 51372142), Innovation Research Group (IRG: 5132109), and the Program of Introducing Talents of Discipline to Universities in China (111 program No. b06015). Hua Tan thanks the financial support by China Scholarship Council (No. 201706220185) for her academic visit to the Nanyang Technological University, Singapore.

Notes and References

[1] a) F.-X. Ma, L. Yu, C.-Y. Xu, X. W. Lou, *Energy Environ. Sci.* **2016**, 9, 862; b) H. Wang, C. Zhu, D. Chao, Q. Yan, H. J. Fan, *Adv. Mater.* **2017**, 29, 1702093; c) V. Augustyn, P. Simon, B. Dunn, *Energy Environ. Sci.* **2014**, 7, 1597.

[2] P. Simon, Y. Gogotsi, B. Dunn, *Science* **2014**, 343, 1210.

[3] a) S. Li, C. Yu, J. Yang, C. Zhao, M. Zhang, H. Huang, Z. Liu, W. Guo, J. Qiu, *Energy Environ. Sci.* **2017**, 10, 1958; b) J. Yang, C. Yu, S. Liang, S. Li, H. Huang, X. Han, C. Zhao, X. Song, C. Hao, P. M. Ajayan, J. Qiu, *Chem. Mater.* **2016**, 28, 5855; c) J. Yang, C. Yu, X. Fan, C. Zhao, J. Qiu, *Adv. Funct. Mater.* **2015**, 25, 2109.

[4] a) P. Simon, Y. Gogotsi, *Nat. Mater.* **2008**, 7, 845; b) J. Yang, C. Yu, X. Fan, J. Qiu, *Adv. Energy Mater.* **2014**, 4, 1400761; c) K. Naoi, *Fuel Cells* **2010**, 10, 825; d) D. Bélanger, L. Brousse, J. W. Long, *The Electrochemical Society Interface* **2008**, 17, 49.

[5] J. Yan, Q. Wang, C. Lin, T. Wei, Z. Fan, *Adv. Energy Mater.* **2014**, 4, 1400500.

[6] a) C. Yuan, J. Li, L. Hou, X. Zhang, L. Shen, X. W. Lou, *Adv. Funct. Mater.* **2012**, 22, 4592; b) L. Huang, D. Chen, Y. Ding, S. Feng, Z. L. Wang, M. Liu, *Nano Lett.* **2013**, 13, 3135; c) M. Kuang, Y. X. Zhang, T. T. Li, K. F. Li, S. M. Zhang, G. Li, W. Zhang, *J. Power Sources* **2015**, 283, 270.

[7] J. Yang, C. Yu, X. Fan, S. Liang, S. Li, H. Huang, Z. Ling, C. Hao, J. Qiu, *Energy Environ. Sci.* **2016**, 9, 1299.

[8] C. Zhu, P. Yang, D. Chao, X. Wang, X. Zhang, S. Chen, B. K. Tay, H. Huang, H. Zhang, W. Mai, H. J. Fan, *Adv. Mater.* **2015**, 27, 4566.

[9] Q. Liao, N. Li, S. Jin, G. Yang, C. Wang, *ACS Nano* **2015**, 9, 5310.

[10] T. Wang, Q. Le, G. Zhang, S. Zhu, B. Guan, J. Zhang, S. Xing, Y. Zhang, *Electrochim. Acta* **2016**, 211, 627.

[11] a) S. Li, D. Wu, C. Cheng, J. Wang, F. Zhang, Y. Su, X. Feng, *Angew. Chem. Int. Ed.* **2013**, 52, 12105; b) Q. Qu, S. Yang, X. Feng, *Adv. Mater.* **2011**, 23, 5574; c) L. Peng, X. Peng, B. Liu, C. Wu, Y. Xie, G. Yu, *Nano Lett.* **2013**, 13, 2151.

[12] a) X. Lu, M. Yu, T. Zhai, G. Wang, S. Xie, T. Liu, C. Liang, Y. Tong, Y. Li, *Nano Lett.* **2013**, 13, 2628; b) T. i. a. I. A. Kosolapova, *Handbook of high temperature compounds: properties, production, applications*, CRC Press, 1990; c) Y. Zhang, B. Ouyang, J. Xu, G. Jia, S. Chen, R. S. Rawat, H. J. Fan, *Angew. Chem. Int. Ed.* **2016**, 55, 8670.

[13] K. Grigoras, J. Keskinen, L. Grönberg, E. Yli-Rantala, S. Laakso, H. Välimäki, P. Kauranen, J. Ahopelto, M. Prunnila, *Nano Energy* **2016**, 26, 340.

[14] a) X. Xiao, X. Peng, H. Jin, T. Li, C. Zhang, B. Gao, B. Hu, K. Huo, J. Zhou, *Adv. Mater.* **2013**, 25, 5091; b) B. Wang, Z. Chen, G. Lu, T. Wang, Y. Ge, *Mater. Res. Bull.* **2016**, 76, 37.

[15] a) G. Ma, Z. Wang, B. Gao, T. Ding, Q. Zhong, X. Peng, J. Su, B. Hu, L. Yuan, P. K. Chu, J. Zhou, K. Huo, *J. Mater. Chem. A* **2015**, 3, 14617; b) L. Chen, C. Liu, Z. Zhang, *Electrochim. Acta* **2017**, 245, 237.

[16] M.-S. Balogun, W. Qiu, W. Wang, P. Fang, X. Lu, Y. Tong, *J. Mater. Chem. A* **2015**, 3, 1364.

[17] Y. Yu, W. Gao, Z. Shen, Q. Zheng, H. Wu, X. Wang, W. Song, K. Ding, *J. Mater. Chem. A* **2015**, 3, 16633.

[18] a) X. Wang, B. Liu, R. Liu, Q. Wang, X. Hou, D. Chen, R. Wang, G. Shen, *Angew. Chem.* **2014**, 126, 1880; b) L. Yuan, X.-H. Lu, X. Xiao, T. Zhai, J. Dai, F. Zhang, B. Hu, X. Wang, L. Gong, J. Chen, C. Hu, Y. Tong, J.

Zhou, Z. L. Wang, *ACS Nano* **2012**, 6, 656; c) Y. He, W. Chen, X. Li, Z. Zhang, J. Fu, C. Zhao, E. Xie, *ACS Nano* **2013**, 7, 174; d) J. Chen, A. I. Minett, Y. Liu, C. Lynam, P. Sherrell, C. Wang, G. G. Wallace, *Adv. Mater.* **2008**, 20, 566.

[19] a) Y. Meng, Y. Zhao, C. Hu, H. Cheng, Y. Hu, Z. Zhang, G. Shi, L. Qu, *Adv. Mater.* **2013**, 25, 2326; b) Z. Xu, C. Gao, *Nat. Commun.* **2011**, 2, 571; c) Z. Dong, C. Jiang, H. Cheng, Y. Zhao, G. Shi, L. Jiang, L. Qu, *Adv. Mater.* **2012**, 24, 1856; d) H.-P. Cong, X.-C. Ren, P. Wang, S.-H. Yu, *Sci. Rep.* **2012**, 2, 613.

[20] Y. Wang, L. Chen, X. Yu, Y. Wang, G. Zheng, *Adv. Energy Mater.* **2017**, 7, 1601390.

[21] B. Cui, H. Lin, Y.-z. Liu, J.-b. Li, P. Sun, X.-c. Zhao, C.-j. Liu, *J. Phys. Chem. C* **2009**, 113, 14083.

[22] Z. Peng, D. Jia, A. M. Al‐Enizi, A. A. Elzatahry, G. Zheng, *Adv. Energy Mater.* **2015**, 5, 1402031.

[23] a) J. Liu, S. Tang, Y. Lu, G. Cai, S. Liang, W. Wang, X. Chen, *Energy Environ. Sci.* **2013**, 6, 2691; b) J. Durst, A. Siebel, C. Simon, F. Hasche, J. Herranz, H. Gasteiger, *Energy Environ. Sci.* **2014**, 7, 2255.

[24] a) K. Xu, P. Chen, X. Li, Y. Tong, H. Ding, X. Wu, W. Chu, Z. Peng, C. Wu, Y. Xie, *J. Am. Chem. Soc.* **2015**, 137, 4119; b) P. Chen, K. Xu, Z. Fang, Y. Tong, J. Wu, X. Lu, X. Peng, H. Ding, C. Wu, Y. Xie, *Angew. Chem.* **2015**, 127, 14923.

[25] H.-S. Kim, J. B. Cook, H. Lin, Jesse S. Ko, Sarah H. Tolbert, V. Ozolins, B. Dunn, *Nat. Mater.* **2016**, 16, 454.

[26] Y. Wang, W. Lai, N. Wang, Z. Jiang, X. Wang, P. Zou, Z. Lin, H. J. Fan, F. Kang, C.-P. Wong, C. Yang, *Energy Environ. Sci.* **2017**, 10, 941.

[27] J. Chang, M. Jin, F. Yao, T. H. Kim, V. T. Le, H. Yue, F. Gunes, B. Li, A. Ghosh, S. Xie, Y. H. Lee, *Adv. Funct. Mater.* **2013**, 23, 5074.

[28] S. Sun, S. Wang, S. Li, Y. Li, Y. Zhang, J. Chen, Z. Zhang, S. Fang, P. Wang, *J. Mater. Chem. A* **2016**, 4, 18646.

[29] H. Ma, J. He, D.-B. Xiong, J. Wu, Q. Li, V. Dravid, Y. Zhao, *ACS Appl. Mater. Interfaces* **2016**, 8, 1992.

[30] H. Chen, T. N. Cong, W. Yang, C. Tan, Y. Li, Y. Ding, *Progress in Natural Science* **2009**, 19, 291.

[31] M. Yan, Y. Yao, J. Wen, L. Long, M. Kong, G. Zhang, X. Liao, G. Yin, Z. Huang, *ACS Appl. Mater. Interfaces* **2016**, 8, 24525.

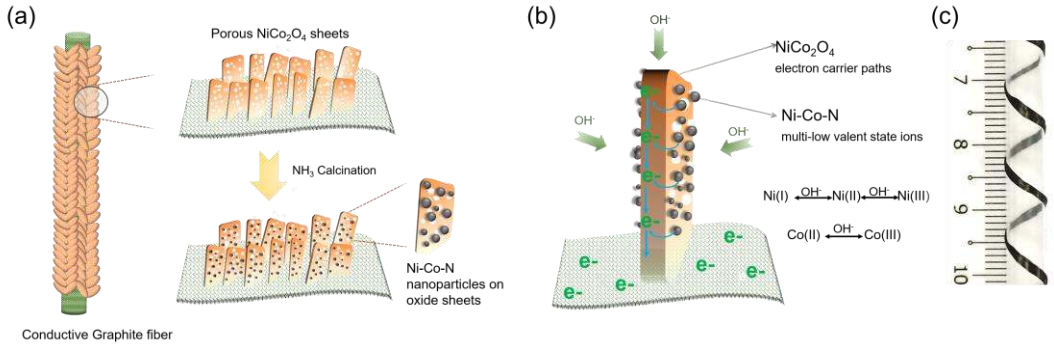

Fig. 1 Schematics of the *in situ* formation for the connected Ni-Co-N/$NiCo_2O_4$/GFs (a), schematic illustration displaying the merits of Ni-Co-N/$NiCo_2O_4$/GFs flexible electrode for energy storage (b), digital images of the pristine flexible graphite fibers wrapped on drinking straw (c).

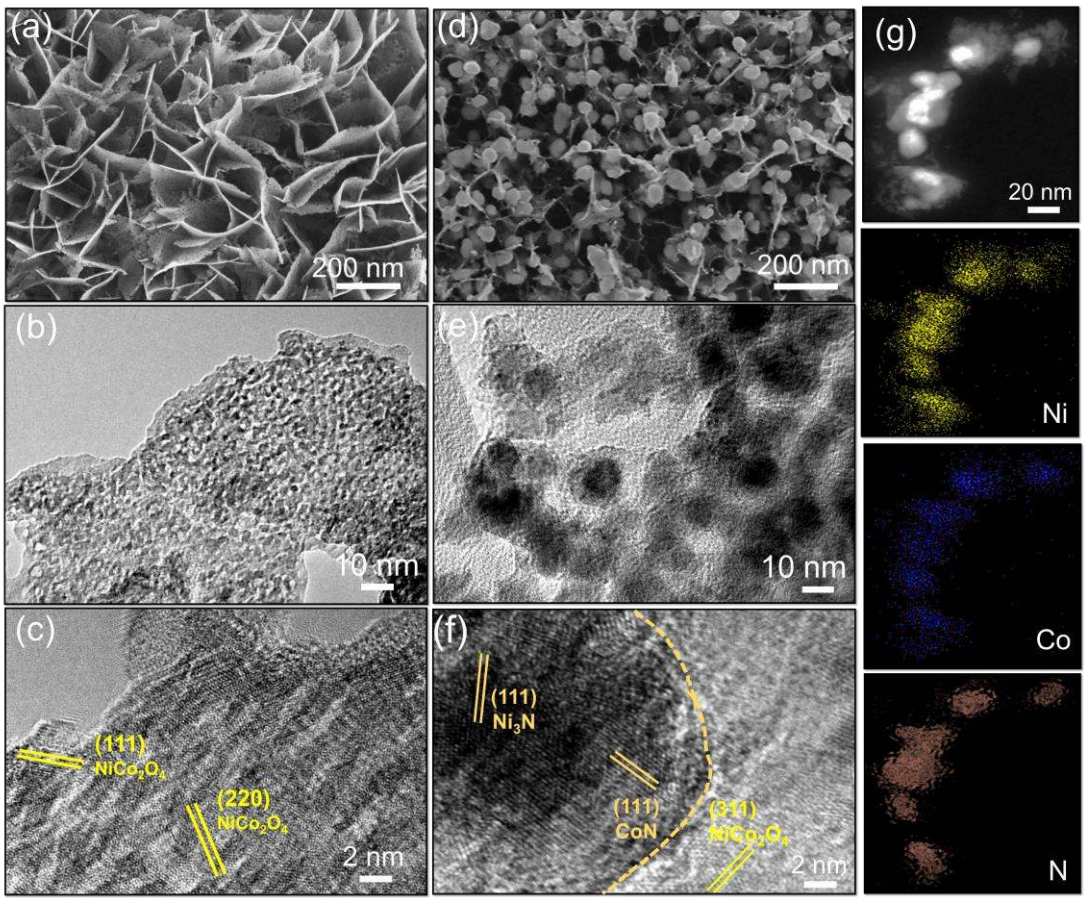

Fig. 2 Nanostructure characterization of the electrode. (a-c) $NiCo_2O_4$ nanosheets vertical grown on graphitic fiber. (d-f) The obtained Ni-Co-N/$NiCo_2O_4$ hybrid after nitridization in ammonia. (g) STEM elemental mappings of the hybrid showing the uniform distribution of Ni, Co, and N.

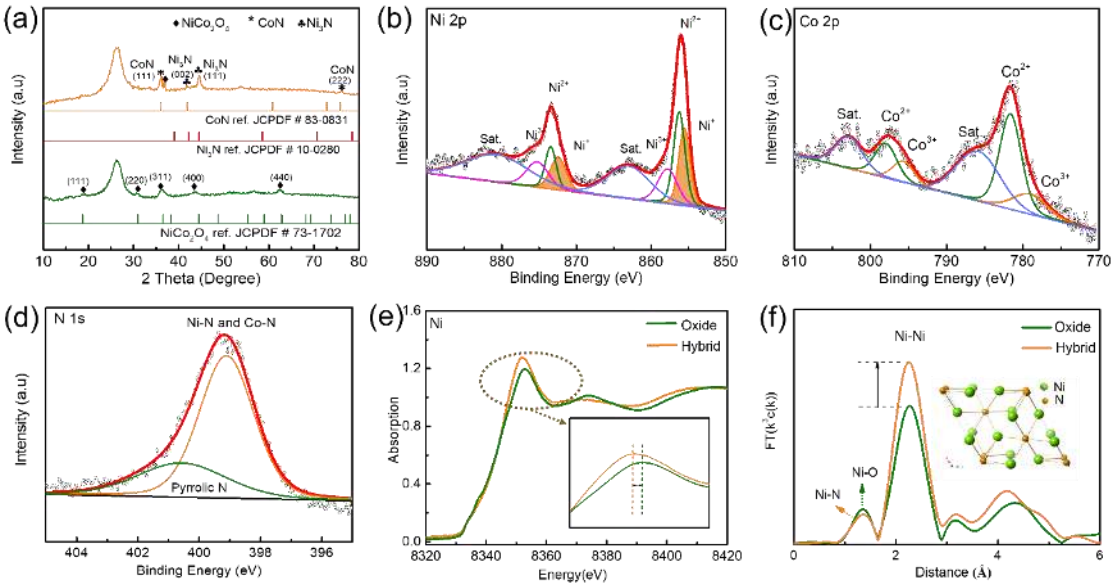

Fig. 3 Chemical composition characterization. XRD patterns (a) of the $NiCo_2O_4$/GFs (Oxide in the figure) and Ni-Co-N/$NiCo_2O_4$/GFs (Hybrid in the figure), high resolution Ni 2p (b) and Co 2p (c) and N1s (d) XPS spectrum of the Ni-Co-N/$NiCo_2O_4$/GFs. Ni K-edge extended XANES spectra (e) and the Fourier transforms of the Ni (f) edge EXAFS spectra (Inset: corresponding crystal structure of Ni_3N). The EXAFS data for Co peak is shown in Supporting Information, Fig. S3.

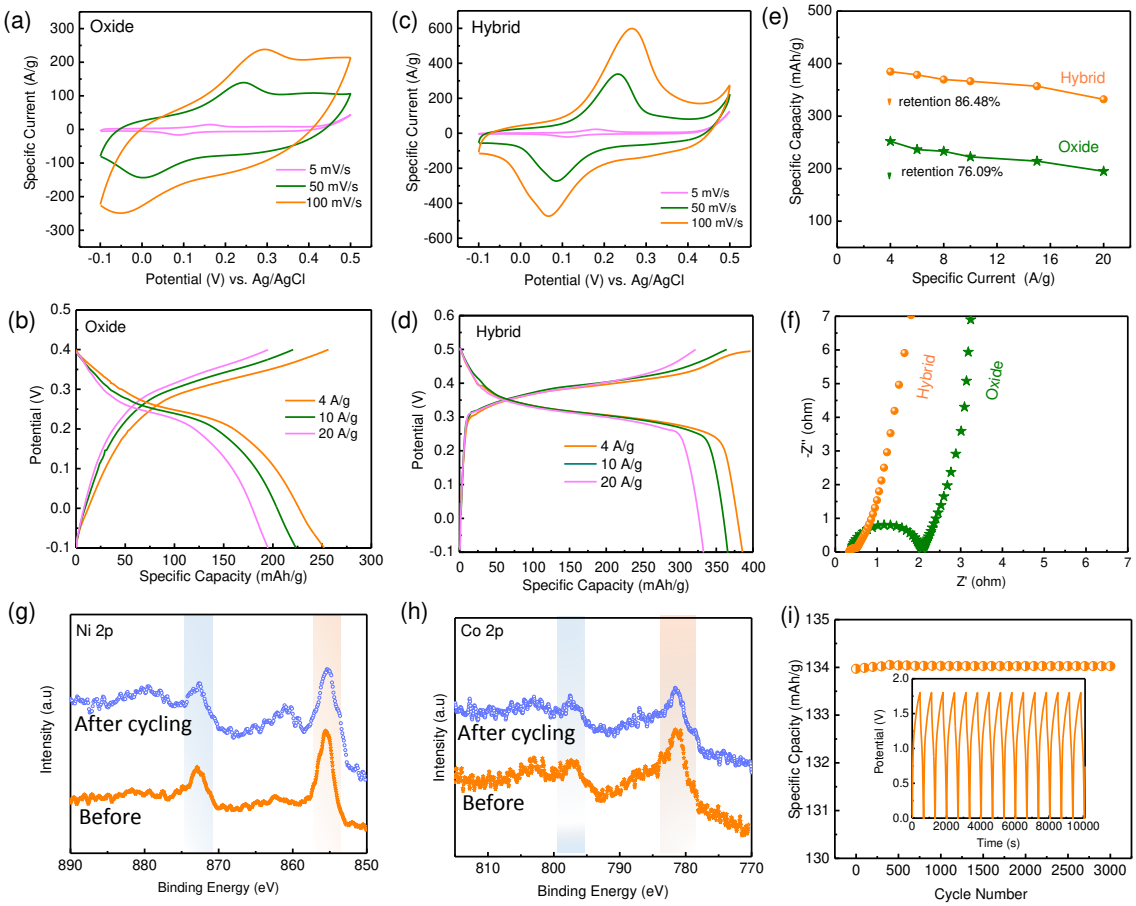

Fig. 4 Electrochemistry of the electrodes. Rate-dependent CV and GCD curves of the (a, b) $NiCo_2O_4$/GFs (Oxide in the figure) and (c, d) and Ni-Co-N/$NiCo_2O_4$/GFs (Hybrid in the figure). (e) Comparison of the specific capacities as a function of specific current for both the pure oxide nanosheet and the nitride-oxide hybrid electrode; (f) Nyquist plots in the frequency range of 10 mHz to 100 kHz of the two electrodes; (i) Cycling stability of the Ni-Co-N/$NiCo_2O_4$/GFs at 8 A/g, the inset shows the GCD curves of the last 15 cycles. High-resolution XPS spectra of (g) Ni 2p, (h) Co 2p of Ni-Co-N/$NiCo_2O_4$/GFs before and after cycling.

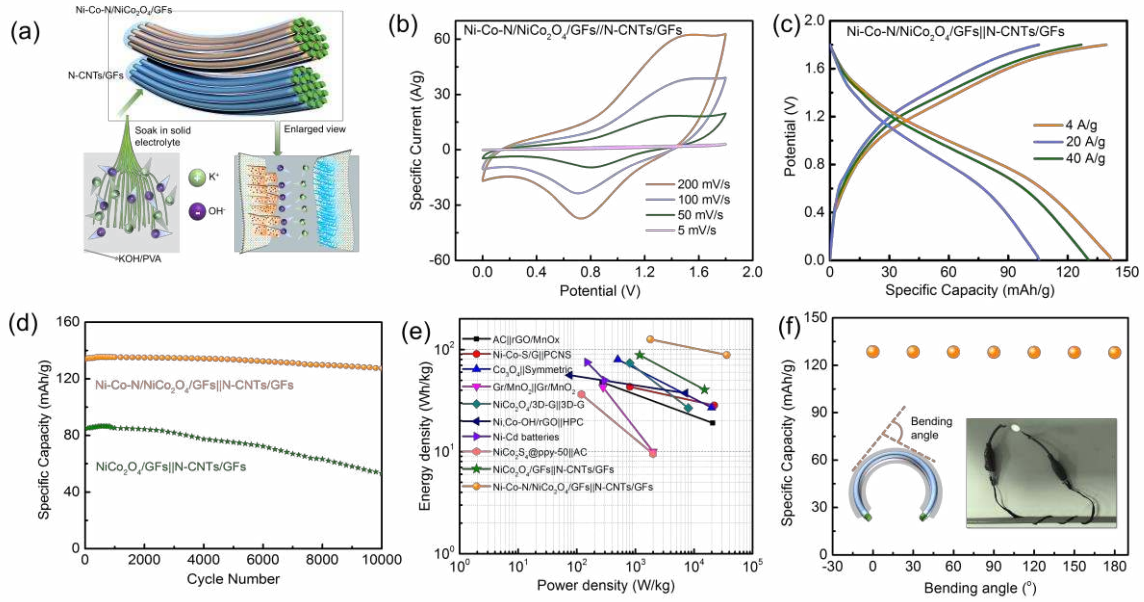

Fig. 5 Performance of asymmetric full cells. (a) Schematic diagram of the fabrication process of solid state flexible device, CV (b) and GCD (c) curves of the Ni-Co-N/$NiCo_2O_4$/GFs||N-CNTs/GFs based device at different scan rates; (d) Cycling stability comparison of two kinds of full devices at a specific current of 8 A/g, (e) Performance comparison of our capacitive asymmetric full device with previously reported capacitive devices, and (f) flexibility performance of the full device based on Ni-Co-N/$NiCo_2O_4$/GFs||N-CNTs/GFs at various bending angles, the inset is the LED lighting using the energy storage device.

Table of Content of Entry

We fabricate a “pearled-veil” hybrid structure containing Ni-Co-N nanospheres anchored within the network of $NiCo_2O_4$ nanosheets on graphite fibers, which show enhanced electrochemical energy storage performance compared to the pure ternary oxide nanosheets electrode. A full solid-state, fiber-shaped device is demonstrated.

Partial Nitridation Induced Electrochemistry Enhancement of Ternary Oxide Nanosheets for Fiber Energy Storage Device